Achieving Superhydrophobicity of Zr-Based Metallic Glass Surfaces with Tunable Adhesion by Nanosecond Laser Ablation and Annealing

Mingming Cui[1], Hu Huang[1], Chao Wang[1], Lin Zhang[2], Jiwang Yan[2]*

KEYWORDS: *metallic glass, nanosecond laser, hierarchical micro/nanostructure, superhydrophobicity, tunable adhesion*

ABSTRACT: Tuning the surface wettability and adhesion of metallic glasses (MGs) is a promising approach to enrich their engineering applications. In this study, using nanosecond laser ablation in air, hierarchical micro/nanostructures were directly fabricated on a Zr-based MG surface. Following subsequent annealing, the surface exhibited superhydrophobicity (maximum contact angle: 166°, minimum sliding angle: 2°). Furthermore, the superhydrophobic surface could be tuned from low to high surface adhesion force by controlling the laser-ablated spot interval. By analyzing the laser-ablated structures and surface chemical compositions, the superhydrophobicity was related to the formation of hierarchical micro/nanostructures and the absorption of organic compounds with low surface free energy in air, and the change in surface adhesion force was attributed to the difference in surface roughness. The experimental results showed that the superhydrophobic surface with low adhesion force could be used in self-cleaning applications, while the superhydrophobic surfaces with different adhesion forces could be used in no-loss liquid transportation. This

study provides an efficient and low-cost way to fabricate superhydrophobic MG surfaces with tunable adhesion, which will broaden the functional applications of MGs.

1. INTRODUCTION

Inspired by the phenomenon of superhydrophobic plants in nature,[1] superhydrophobic surfaces with water contact angles (CAs) larger than 150° have attracted much attention in daily life, industrial engineering and scientific research. As two typical superhydrophobic surfaces in nature, lotus leaf[2] and rose petal[3] show very different water adhesion behaviors. The lotus leaf exhibits low adhesion to water, such that water droplets easily slide from its surface. Superhydrophobic surfaces with low adhesion could be applied in anti-icing, drag reduction and self-cleaning applications.[4-6] In contrast, the rose petal exhibits high adhesion to water, where water droplets tightly contact with its surface. Superhydrophobic surfaces with high adhesion are suitable for no-loss liquid transportation, microfluidic systems and water collection.[1,7-9]

Due to the difference in atomic arrangement compared to that of conventional alloys and metals, metallic glasses (MGs) possess unique mechanical, physical, and chemical properties,[10-12] and thus are considered promising structural and functional materials. Achieving superhydrophobicity of MG surfaces with tunable adhesion is important to broaden their functional applications. Superhydrophobic surface tendency is closely related to the surface's structure and free energy. Therefore, to achieve superhydrophobicity of MGs, many technologies have been developed. For example, by using an electrochemical method and chemical modification,[13] coral-like micro/nanostructures were prepared on Zr-based MG, which exhibited superhydrophobicity with low adhesion. Based on thermoplastic forming

technology,[14] hierarchical micro/nanostructures were generated on Pd-based MG, which showed superhydrophobicity with high adhesion. Via laser texturing and heat treatment,[15] the superhydrophobic surface was fabricated on Zr-based MG. Among the aforementioned technologies, laser texturing technology is promising due to its high efficiency and environmental friendliness.[16,17] In particular, compared with picosecond and femtosecond pulse lasers, nanosecond pulse lasers are suitable for the industrialized application of laser texturing technology because they cost less and are more efficient. However, tuning the adhesion of superhydrophobic MG surfaces by using a nanosecond laser has not been investigated until now.

In this study, hierarchical micro/nanostructures were directly fabricated on a Zr-based MG surface by nanosecond laser ablation in air. Via a subsequent low-temperature annealing treatment, the surface developed a superhydrophobic tendency. Furthermore, by controlling the spot interval (*SI*), superhydrophobic MG surfaces with tunable adhesion were achieved, and the corresponding mechanisms were investigated by analyzing the surface morphologies, three-dimensional (3D) topographies, X-ray diffraction (XRD) and X-ray photoelectron spectroscopy (XPS) results. Finally, the potential applications of superhydrophobic surfaces in self-cleaning and no-loss liquid transportation were experimentally verified.

2. EXPERIMENTAL METHODS

2.1. Materials. $Zr_{41.2}Ti_{13.8}Cu_{12.5}Ni_{10}Be_{22.5}$ (at.%) sheets with dimensions of 20 mm × 20 mm × 2 mm were used. Before laser ablation, the sheets were mechanically polished to a mirror-like finish with a surface roughness of ~10 nm.

2.2. Laser Ablation and Annealing. The MG samples were ablated using a nanosecond laser

(wavelength: 1064 nm, pulse width: 230 ns, polarization direction: circular polarization, repetition frequency: 50 kHz) in ambient air. The laser processing path is illustrated in Figure S1, and the diameter of the laser beam focused on the sample was ~43 μm. To introduce hierarchical micro/nanostructures on the MG surface, the employed irradiation time and peak laser power intensity were 2 ms and 2.6×10^{11} W/m^2, respectively, following a range of pre-experimental studies. Five *SI*s, 50, 70, 90, 110 and 130 μm, were selected in subsequent experiments to investigate the effects of surface roughness on surface wettability. After laser ablation, the samples were annealed in a drying box at 100°C for 12 hours. The aforementioned experimental parameters are summarized in Table 1.

Table 1. Experimental parameters.

Sample material	$Zr_{41.2}Ti_{13.8}Cu_{12.5}Ni_{10}Be_{22.5}$ (at.%)
Laser wavelength (nm)	1064
Pulse width (ns)	230
Polarization direction	Circular polarization
Pulse repetition frequency (kHz)	50
Beam diameter (μm)	~43
Irradiation time (ms)	2
Peak laser power intensity ($\times 10^{11}$ W/m^2)	2.6
Spot interval (*SI*) (μm)	50, 70, 90, 110, 130

Atmosphere	Air
Annealing condition	100℃ (12 hours)

2.3. Morphologies and Wettability of the Laser-Ablated Surfaces. The morphologies of the laser-ablated surfaces were observed by field emission scanning electron microscopy (FESEM, SU8010, Hitachi, Japan). The surface three-dimensional (3D) topographies were measured using a white light interferometer (Zygo NewView 9000, Ametek, USA). The contact angle (CA) and sliding angle (SA) of the laser-ablated surfaces were measured by contact angle meter (OSA60, NBSI, China) with 5 μL water before and after annealing. The adhesion force of the superhydrophobic surface was tested using a surface analyzer (LSA100, LAUDA Scientific, Germany). The typical measurement processes of the adhesion force are shown in Figure S2. First, a water droplet was hung on the needle tip. Then, the superhydrophobic surface was moved up to contact the water droplet until the water droplet was compressed by a certain amount. Next, the superhydrophobic surface was moved down until the water droplet and surface were completely separated. The force between the water droplet and material surface in the vertical direction could be accurately calculated by the analysis software, which used an embedded theoretical algorithm. The maximum tensile force was defined as the adhesion force between the water droplet and the surface.

2.4. Chemical Compositions of the Laser-ablated Surfaces. The chemical compositions of the laser-ablated surfaces were analyzed using X-ray diffraction (XRD, D8 Discover, Bruker, Germany) and X-ray photoelectron spectroscopy (XPS, ESCALAB 250Xi, Thermo Fisher, USA) before and after annealing.

3. RESULTS AND DISCUSSION

3.1. Laser-Ablated Surfaces. Figure 1 shows the morphologies of the laser-ablated region obtained under an irradiation time of 2 ms and a peak laser power intensity of 2.6×10^{11} W/m^2, as imaged using FESEM. As shown in Figure 1a, a crater formed on the MG surface. Figures 1b-f display locally enlarged views corresponding to regions 1-5 in Figure 1a, which exhibit more detailed microfeatures of the crater. Nanoparticles were generated in regions 1, 2 and 4, and ripple-like features appeared in region 5. In addition, microcracks developed in region 3. Figure 1g shows the 3D topography of the crater, and Figure 1h shows the cross-sectional profile of the white dotted line in Figure 1g. The width of the heat-affected zone and the diameter of the crater were ~90 μm and ~47 μm, respectively. The height of resolidification and the depth of the crater were ~3 μm and ~25 μm, respectively. The above results indicate that a hierarchical micro/nano-crater was successfully generated in the laser-ablated region.

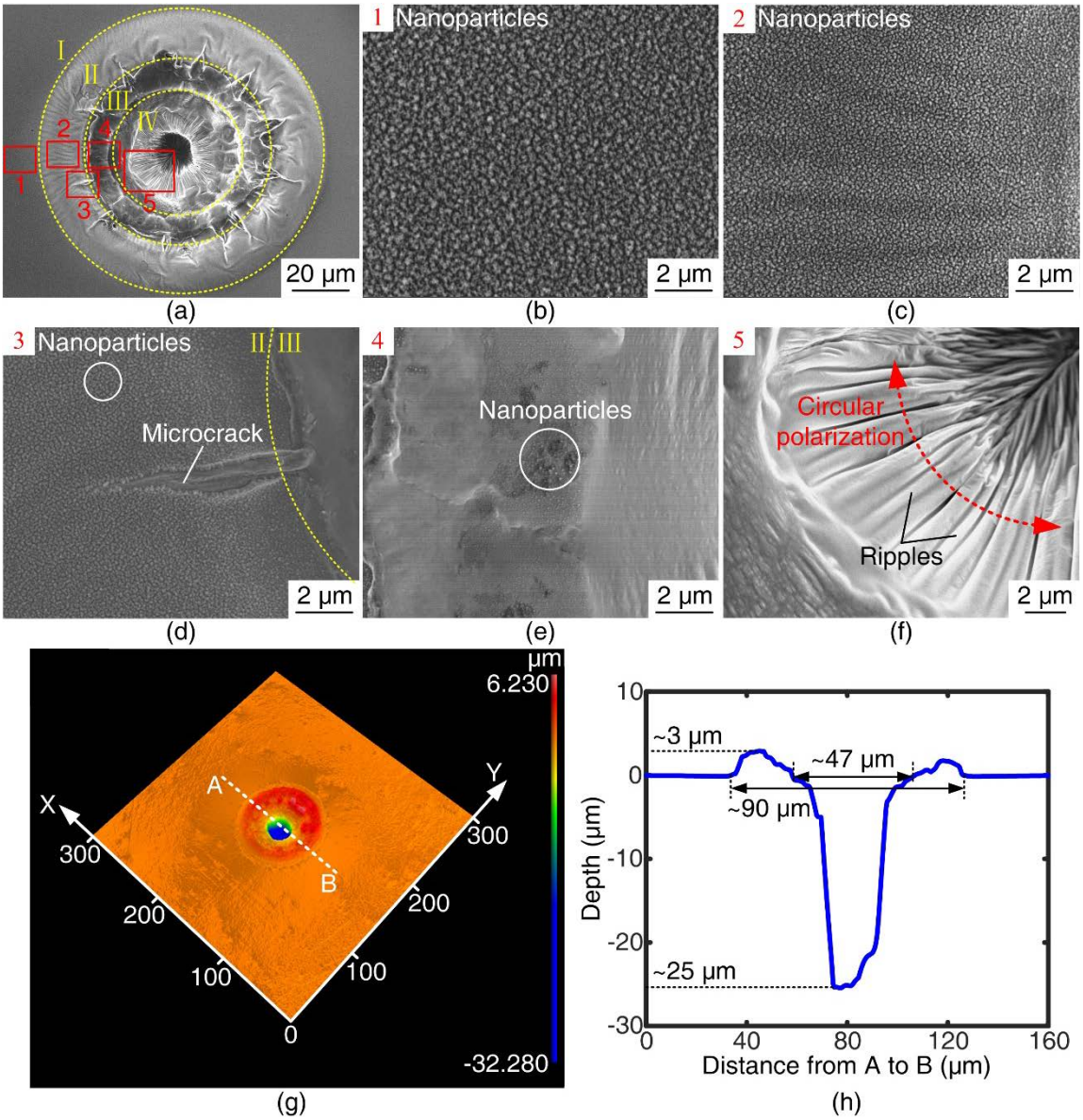

Figure 1. (a) Morphology of a hierarchical micro/nano-crater obtained under a peak laser power intensity of 2.6×10^{11} W/m^2, as imaged using FESEM. (b)-(f) Locally enlarged microfeatures of regions 1-5 in (a). (g) 3D topography of the crater. (h) Cross-sectional profile of the white dotted line in (g).

In Figure 1, the hierarchical micro/nanoscale crater mainly possesses three kinds of features: microcracks, nanoparticles, and ripples. The microcracks, which were induced by tensile stress, were reported in our previous study.[18] The possible formation mechanisms of

nanoparticles and ripples are illustrated in Figure S3. Nanosecond pulse laser ablation is a thermal process, during which the laser-ablated region rapidly melts and evaporates when the peak laser power intensity reaches the ablation threshold. Therefore, the metal vapor could eject from the center to the surroundings of the crater due to the recoil pressure. Once the metal vapor drops in the relatively low-temperature region, nanoparticles are formed. In addition, the incident light reaches the smooth inner wall of the crater and then reflects to the other side of the inner wall. The reflected light intervenes with the incident light, inducing the formation of ripples.[19,20] In general, the direction of the laser-induced ripples is perpendicular to the laser polarization direction,[21-24] and the result shown in Figure 1f is in agreement with this theory.

By moving the laser beam along the processing path (see Figure S1), crater arrays were fabricated on the MG surface. Figure 2 shows the morphologies of the laser-ablated surfaces obtained when the *SI* changes from 50 to 130 μm, as imaged using FESEM. Because the width of the heat-affected zone of the crater was ~90 μm, the region around the crater was ablated by the subsequent laser beams when the *SI* was smaller than 90 μm. Therefore, as shown in Figures 2a and d, the thermal effect among the laser-ablated craters was relatively large when the *SI*s were 50 and 70 μm, resulting in the relatively rough morphologies of the laser-ablated surfaces. In contrast, when the *SI*s were 90, 110, and 130 μm, the flat regions occupied a relatively large ratio of the laser-ablated surface, as shown in Figures 2g, j and m. In contrast to the morphology in Figure 1f, nanoparticles distributed on the ripples were also observed, as shown in Figures 2c, f, i, l, and o. This is because the nanoparticles were ejected by laser ablation and then deposited on the previously formed ripples. Because of the

relatively large ejection radius of the nanoparticles, the laser-ablated surfaces were covered with nanoparticles during laser array machining. Accordingly, typical hierarchical micro/nanostructures were fabricated on the MG surface. Furthermore, the number of laser-ablated craters decreased per unit area when the *SI* was increased from 50 to 130 μm, and the distribution density of nanoparticles obviously decreased, as well.

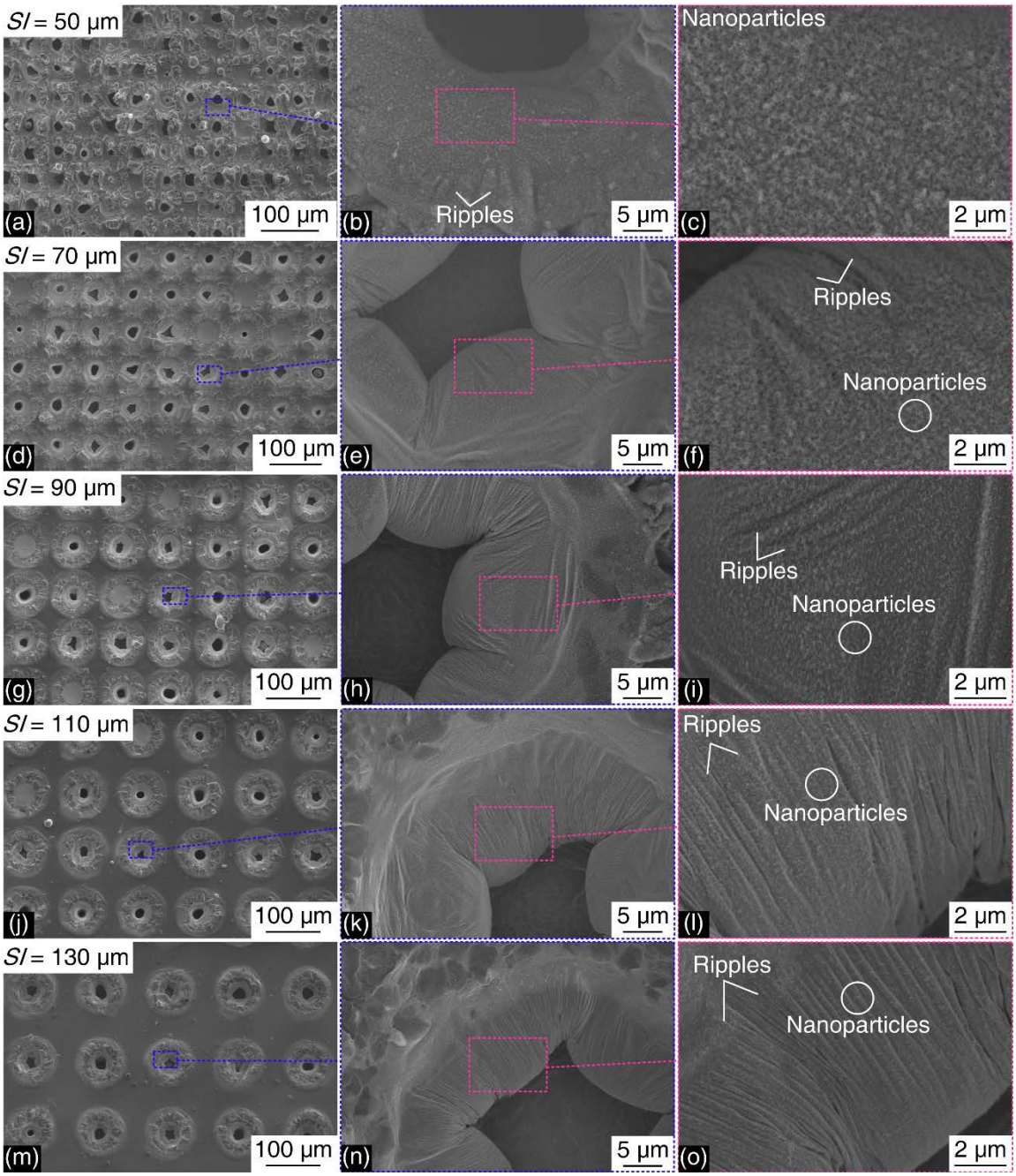

Figure 2. Morphologies of the laser-ablated surfaces (imaged using FESEM) obtained under

different *SI*s: (a)-(c) *SI* = 50 μm, (d)-(f) *SI* = 70 μm, (g)-(i) *SI* = 90 μm, (j)-(l) *SI* = 110 μm, and (m)-(o) *SI* = 130 μm.

By observing the surface morphologies in Figure 2, the laser-ablated surfaces obtained under different *SI*s were found to exhibit different roughness. Therefore, it was necessary to further investigate the effect of *SI* on the surface roughness. Figure S4 shows the 3D topographies of the laser-ablated surfaces obtained under different *SI*s, and the surface roughness, Sa, values were 5.055, 3.431, 2.124, 1.823 and 1.374 μm when the investigated *SI*s were 50, 70, 90, 110 and 130 μm, respectively. The results indicate that the surface roughness decreases with the increase of *SI*, which agrees well with the surface morphologies in Figure 2.

3.2. Surface Wettability. Figure S5 shows the CAs of the laser-ablated surfaces obtained under different *SI*s. For comparison, the CA of the polished surface (85°) is also included, as shown in Figure S5f. This value indicated that the polished surface was inherently hydrophilic. After laser ablation, all the CAs of the laser-ablated surfaces were ~0°, as shown in Figures S5a-e and Movies S1 and 2, which demonstrates the excellent superhydrophilicity of the surface. The above results indicate that the hierarchical micro/nanostructures are able to effectively tune the surface wettability, which can be explained by the Wenzel model:[25]

$$\cos\theta_W = r\cos\theta \quad (1)$$

where θ_W is the CA of the laser-ablated surface, θ is the CA of the polished surface, and r is the surface roughness factor. For the hydrophilic surface, the r decreases with increasing surface roughness. Therefore, the increase in surface roughness converts a hydrophilic polished surface (CA: 85°) into the superhydrophilic surface (CA: ~0°).

Previous studies[15,26-28] have shown that a superhydrophilic surface ablated by laser can be transformed into a superhydrophobic surface by annealing. Therefore, by using a low-temperature annealing treatment, the possibility of this transition from superhydrophilicity to superhydrophobicity was further investigated. Figure S6 shows the CAs of the laser-ablated surfaces as well as the polished surface after annealing. As shown in Figures S6a-e, all the surfaces achieved superhydrophobicity. The CAs were 166°, 163°, 157°, 153° and 151° when the *SIs* were 50, 70, 90, 110 and 130 μm, respectively. As shown in Figure S6f, the CA of the polished surface after annealing was 104°, which was larger than that of the original polished surface. By annealing, the hydrophilic polished surface (CA: 85°) achieved hydrophobicity (CA: 104°) rather than superhydrophobicity, indicating that the hierarchical micro/nanostructures formed by laser ablation played an important role in achieving superhydrophobicity.

Furthermore, the contact state between the water droplet and the surface, as shown in Figure S6, satisfies the Cassie-Baxter model:[29]

$$\cos\theta_{CB} = f_s(\cos\theta_Y + 1) - 1 \quad (2)$$

where θ_{CB} is the CA of the laser-ablated surface after annealing, θ_Y is the CA of the polished surface after annealing, and f_s is the area fraction between the solid surface and the liquid surface. When θ_{CB} = 166° and θ_Y = 104°, f_s is calculated to be 3.91%. Therefore, only 3.91% of the surface of the water droplet contacts with the superhydrophobic surface (*SI* = 50 μm). Furthermore, when the *SI* was increased to 70, 90, 110, or 130 μm, the f_s was calculated to be 5.76%, 10.49%, 14.38%, or 16.54%, respectively. The above results demonstrate that the contact ratio between the water droplet and the superhydrophobic surface increased with

increasing *SI*. Furthermore, by analyzing the surface morphology and roughness of the superhydrophobic surface, it is concluded that the rough surface structure is able to reduce the contact area between the water droplet and the superhydrophobic surface. Figure 3a shows the CAs of the laser-ablated surfaces obtained before and after annealing under different *SI*s. It can be clearly seen that the laser-ablated surface is transformed from superhydrophilicity to superhydrophobicity by annealing. The associated wettability transition mechanism is further discussed in Section 3.3.

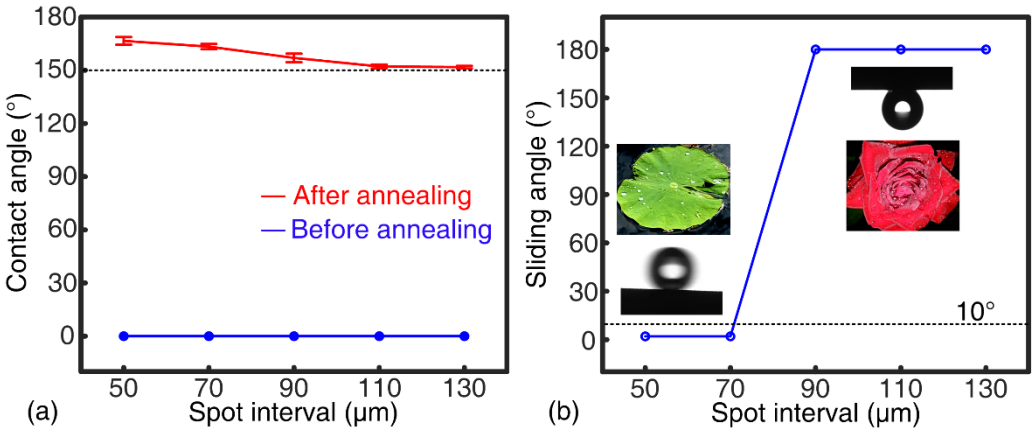

Figure 3. (a) The CAs of the laser-ablated surfaces obtained before and after annealing under different *SI*s. (b) The SAs of the superhydrophobic surfaces obtained under different *SI*s.

Although the laser-ablated surfaces obtained under different *SI*s achieved superhydrophobicity by annealing, it was found that for different *SI*s, the adhesion between the water droplet and the superhydrophobic surface varied during the measurement of the CA. As shown in Figure S7, the superhydrophobic surfaces obtained under different *SI*s were first raised to contact with the water droplet and then dropped down to their original position. When the *SI*s were 50 and 70 μm, the water droplets could not adhere to the surfaces, as shown in Figure S7a, which shows an example of low adhesion. In contrast, the

superhydrophobic surfaces exhibited high adhesion to the water droplet when the *SI*s were 90, 110, and 130 μm, as shown in Figure S7b.

Furthermore, to characterize the difference in surface adhesion, the sliding angles (SAs) of the superhydrophobic surfaces obtained under different *SI*s were measured. Figure 3b shows the results. When the *SI*s were 50 and 70 μm, the SAs were approximately 2°, similar to the behavior of a lotus leaf.[2] The water droplets were able to easily slide from the superhydrophobic surfaces (*SI* = 50, 70 μm) with a tiny sloping angle, indicating that the superhydrophobic surface with a small SA of approximately 2° could be useful in self-cleaning applications. However, when the *SI*s were 90, 110, and 130 μm, the water droplets adhered tightly to the superhydrophobic surfaces. Even when the MG sample was tilted 180°, the water droplet was not able to slide from the surface, similar to the behavior of a rose petal.[3]

To further confirm the differences in adhesion of the superhydrophobic surfaces obtained under different *SI*s, the surface adhesion forces of the various surfaces were measured. Figures 4a and b show the force curves corresponding to different *SI*s. As shown in Figure 4a, when the *SI*s were 50 and 70 μm, the adhesion forces were 18.7 and 22.6 μN, respectively. That is, the superhydrophobic surfaces obtained under *SI*s of 50 and 70 μm exhibited low adhesion. In contrast, the superhydrophobic surfaces obtained under *SI*s of 90, 110, and 130 μm exhibited relatively high adhesion. As shown in Figure 4b, when the *SI*s were 90, 110 and 130 μm, the adhesion forces were 52.9, 56.7 and 58.5 μN, respectively. The above results demonstrate that the superhydrophobic surfaces obtained under different *SI*s exhibited different adhesion forces, which could be useful in no-loss liquid transportation applications.

Furthermore, the source of this difference in adhesion is illustrated in Figures 4c and d. As shown in Figure 4c, the laser-ablated MG surfaces were relatively rough when the *SI*s were 50 and 70 μm, which allowed air to be trapped between the water droplet and the rough micro/nanostructures when the water droplet contacted with the MG surfaces. The air has a low adhesion to water droplets,[30] which in this study presented as a barrier that protected the water droplet from contacting with the MG surfaces. Therefore, the existence of air at the solid-liquid interface played an important role in achieving a low adhesion surface. However, when the *SI* was increased to 90, 110, and 130 μm, the proportion of the flat regions that were not ablated by laser increased, as well. As illustrated in Figure 4d, the water droplet was able to directly contact with these flat regions. The air trapped between the water droplet and the ablated surface was decreased, which resulted in high adhesion. The above results reveal that the rough surface structures play an important role in reducing the adhesion of the superhydrophobic surfaces.

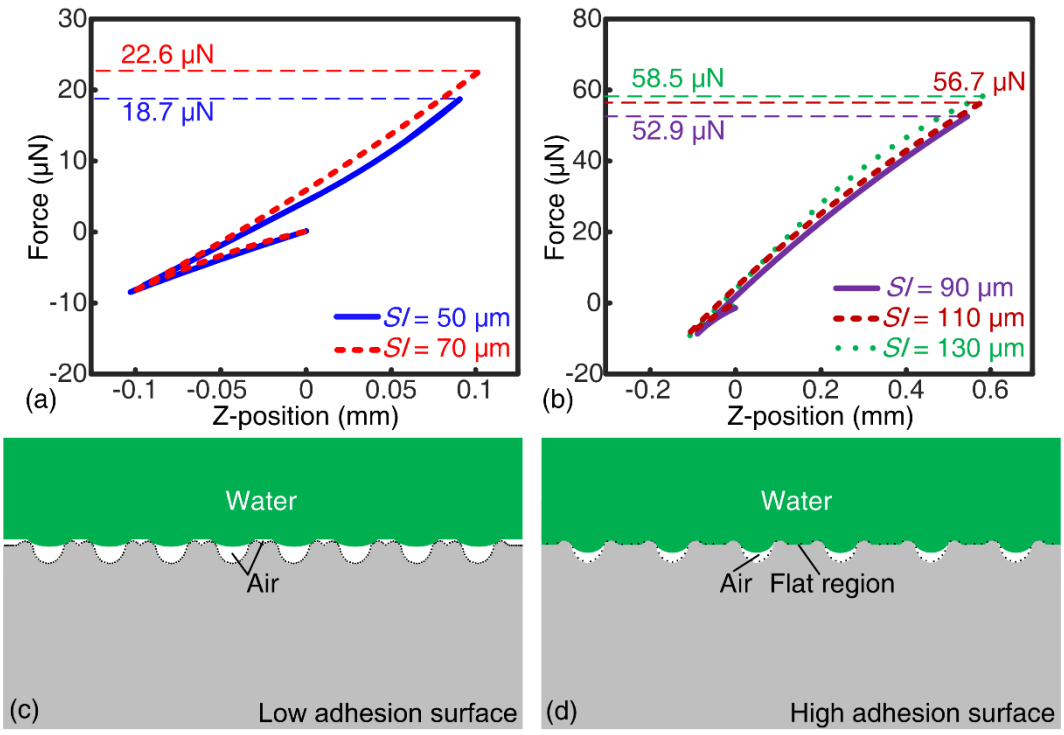

Figure 4. The force between the water droplet and the superhydrophobic surface changes with the position of the superhydrophobic surface: (a) *SI* = 50, 70 μm, and (b) *SI* = 90, 110, 130 μm. Schematic diagrams illustrating the water droplet on (c) the low adhesion surface and (d) the high adhesion surface.

3.3. Surface Chemical Composition Analysis. The polished MG surfaces after laser ablation achieved superhydrophilicity, and the introduction of hierarchical micro/nanostructures was one reason for this, as discussed in Section 3.2. Additionally, the change in surface chemical composition also contributed to the change in surface wettability.[31] For example, metallic oxides have high surface free energy,[32] and thus their introduction would be expected to greatly improve the surface hydrophilicity. Therefore, it was necessary to further characterize the chemical composition of the MG surface before and after laser ablation. Figure 5a shows the XRD results. The polished surface exhibited a typical amorphous feature, but some crystalline phases, such as ZrO_2, TiO_2, CuO, Zr_2Cu, and $Cu_{10}Zr_7$, were detected on the laser-ablated surface (*SI* = 50 μm).[33-37] The formation of metallic oxides (ZrO_2, TiO_2, and CuO) was another possible source of the superhydrophilicity of the laser-ablated surfaces. Accordingly, achieving superhydrophilicity of Zr-based MG surfaces by nanosecond laser ablation depends on the formation of both hierarchical micro/nanostructures and metallic oxides.

After annealing, the laser-ablated surfaces were transformed from superhydrophilic to superhydrophobic. According to several previous studies,[38-40] the metallic oxide transition from CuO to CuO_2 might explain this transition in surface wettability. To investigate whether annealing leads to a metallic oxide transition from CuO to CuO_2, the phases of the laser-

ablated surface before and after annealing were analyzed using XRD. As shown in Figure 5a, there was no obvious change in the metallic oxide phase on the laser-ablated surface before and after annealing, indicating that the surface wettability transition was independent of the metallic oxide transition from CuO to CuO_2. To clarify the wettability transition mechanism, the chemical composition of the laser-ablated surface before and after annealing was further analyzed by XPS. Table S1 and Figure 5b show the XPS results of the surface element content and atom ratio, respectively. The results demonstrate that the content of metallic elements on the laser-ablated surface caused no significant changes to properties before versus after annealing, although the atomic ratios of C/Zr and O/Zr did change significantly. The increase in the O/Zr atom ratio was ascribed to surface oxidation during annealing, and the increase in the C/Zr atom ratio may be related to the absorption of organic compounds from the air during annealing.

To confirm whether the wettability transition from superhydrophilicity to superhydrophobicity could be attributed to the absorption of organic compounds in air, high-resolution C 1s spectra of the laser-ablated surface (SI = 50 μm) before and after annealing were further investigated. As shown in Figure 5d, the high-resolution C 1s spectra present three peaks at approximately 284.8, 286.3, and 288.5 eV, which correspond to the C-C/C-H, C-O, and C=O groups,[41-43] respectively. According to several previous studies,[44,45] the above groups are associated with alkyl, ether, and carboxyl/ester substances in air, confirming that the increase in the C/Zr atom ratio was related to the absorption of organic compounds from the air during annealing. Furthermore, it was necessary to investigate which group played an important role in this wettability transition. Therefore, the characteristics of these three

groups and their percentages on the laser-ablated surface were analyzed further. The C-C/C-H group is nonpolar,[41,44,46,47] which is beneficial to surface hydrophobicity. The percentages of nonpolar C-C/C-H group on the laser-ablated surface before and after annealing were 74.4% and 78.4%, respectively. In contrast, both C-O and C=O are polar groups,[48-51] which are beneficial to surface hydrophilicity. The sums of the percentages of polar C-O and C=O groups on the laser-ablated surface before and after annealing were 25.6% and 21.6%, respectively. Furthermore, Figure 5f shows the atom ratios of nonpolar C-C/C-H, as well as the sum of polar C-O and C=O groups to Zr element of the laser-ablated surface (*SI* = 50 μm) before and after annealing. The atom ratio of nonpolar C-C/C-H group to Zr increased significantly, while the sum of polar C-O and C=O groups to Zr increased only slightly. These results indicated that the percentage of hydrophobic group increased, while the percentage of hydrophilic group decreased after annealing. Based on the above results, the wettability transition from superhydrophilicity to superhydrophobicity can be ascribed to the increase in the percentage of nonpolar C-C/C-H group on the laser-ablated surface after annealing.

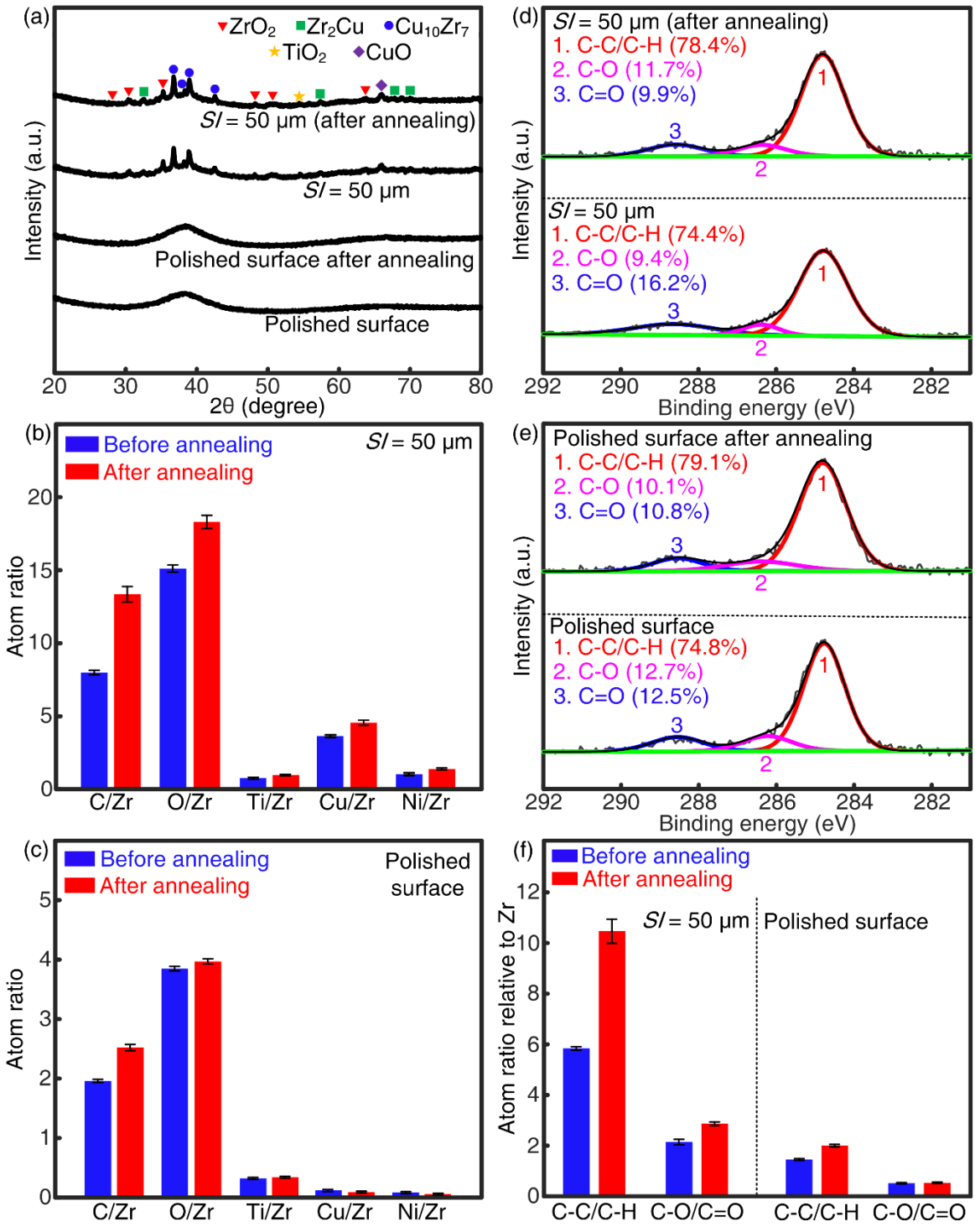

Figure 5. (a) XRD patterns of the polished and laser-ablated surfaces before and after annealing. Atom ratio: (b) the laser-ablated surface (*SI* = 50 μm) and (c) polished surface before and after annealing. High-resolution C 1s spectra before and after annealing: (d) the laser-ablated surface (*SI* = 50 μm) and (e) polished surface. (f) Atom ratios of nonpolar C-

C/C-H, as well as the sum of polar C-O and C=O groups to Zr element of the laser-ablated surface (*SI* = 50 μm) and polished surface before and after annealing.

As the control group, the polished surface was also characterized by XRD and XPS before and after annealing. As shown in Figure 5a, the amorphous state of the polished surface did not change after annealing. However, the hydrophilic polished surface (CA: 85°) achieved hydrophobicity (CA: 104°) after annealing. Furthermore, by analyzing the XPS results, the atom ratio of C/Zr showed a significant change compared with the other atom ratios after annealing, as shown in Figure 5c. In addition, based on the results shown in Figures 5e and f, it can be concluded that the percentage of nonpolar C-C/C-H group increased on the polished surface after annealing. The above XPS results were similar to the results of the laser-ablated surface after annealing, indicating that the wettability transition of the polished surface from hydrophilicity to hydrophobicity could be ascribed to the increase in the percentage of nonpolar C-C/C-H group on the polished surface after annealing, which demonstrated that achieving superhydrophobicity by subsequent annealing was inseparable from the hierarchical micro/nanostructures on the laser-ablated surface.

3.4. Potential Applications of the Superhydrophobic Surface. As shown in Figure S6a, the superhydrophobic surface obtained under the *SI* of 50 μm presented a very large CA (166°) with 5 μL water, demonstrating its excellent ability to resist water. However, if the superhydrophobic surface would also demonstrate an excellent ability to resist a larger volume of water and different kinds of liquid droplets, it would be more meaningful for practical applications. Therefore, the superhydrophobic surface obtained under the *SI* of 50 μm was used to investigate whether the surface also possessed the ability to resist a larger

volume of water and different kinds of liquid droplets. As shown in Figure 6a, both 20 and 40 μL water droplets maintained a nearly spherical shape on the superhydrophobic surface; when the volume of the water droplets was increased to 60 and 80 μL, the water droplets maintained a nearly hemispherical shape with the action of excessive gravity. The above results indicated that the superhydrophobic surface had an excellent ability to resist water. In addition, the orange juice, red ink, and green tea droplets also maintained a nearly spherical shape on the superhydrophobic surface, as shown in Figure 6b, which further verified that the superhydrophobic surface had an excellent ability to resist different kinds of liquid droplets.

In addition, the superhydrophobic surface obtained under the *SI* of 50 μm shows a small SA (2°), as shown in Figure 3b, which could be used in self-cleaning applications. For example, NaCl powder is regarded as a contaminant in self-cleaning experiments. As shown in Figure 6c, the superhydrophobic surface with an inclination angle of 10° was covered with NaCl powder. Then, the water droplets were slowly dropped onto the surface covered with NaCl powder. The NaCl powder was removed by the falling water droplets, as shown in Figures 6d and e. Finally, the superhydrophobic surface covered with NaCl powder was cleaned by the water droplets, as shown in Figure 6f, but the superhydrophobic surface was not wetted by the water droplets. The above results indicated that the superhydrophobic surface (*SI* = 50 μm) with a small SA (2°) had an excellent self-cleaning ability.

Furthermore, as shown in Figures 4a and b, the superhydrophobic surfaces obtained under different *SI*s exhibited different adhesion forces, which could be useful in no-loss liquid transportation applications. As shown in Figure 6g, 2 μL water was dropped on the superhydrophobic surface (*SI* = 50 μm) with a low adhesion force, and then the

superhydrophobic surface (*SI* = 130 μm) with a high adhesion force was moved down to contact with the water droplet, as shown in Figures 6h and i. Next, the superhydrophobic surface (*SI* = 130 μm) was moved up, as shown in Figure 6j. Finally, the water droplet achieved no-loss liquid transportation, as shown in Figure 6k.

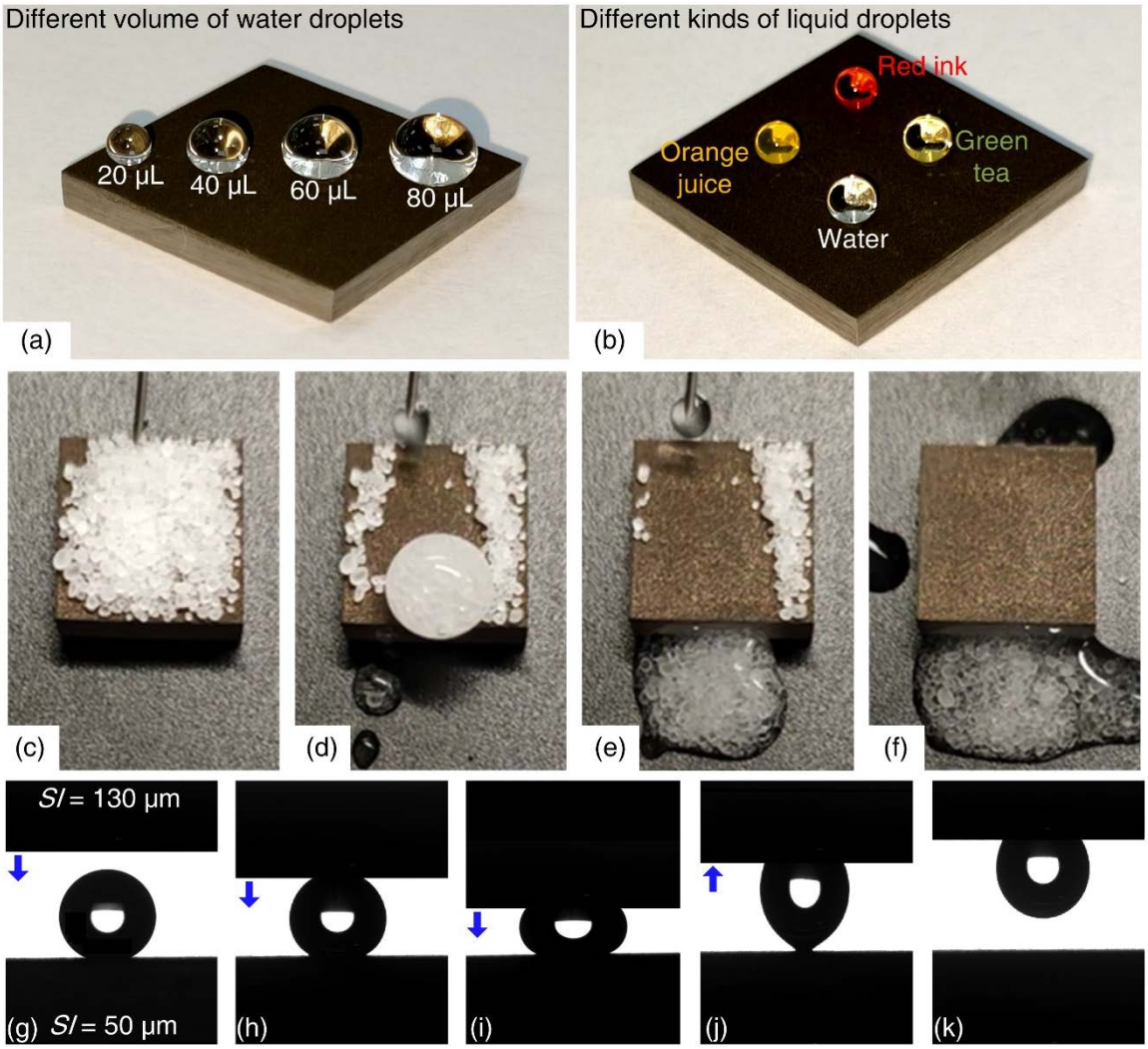

Figure 6. Optical images of (a) different volumes of water and (b) different kinds of liquid droplets on the superhydrophobic surface obtained under the *SI* of 50 μm. (c)-(f) Superhydrophobic surface in a self-cleaning application. (g)-(k) Superhydrophobic surfaces with different adhesion forces in a no-loss liquid transportation application.

4. CONCLUSIONS

In summary, the surface wettability and adhesion of Zr-based MG were tuned using nanosecond laser ablation in air. Via experiments and analysis, the following conclusions were drawn.

(1) After nanosecond laser ablation in air, hierarchical micro/nanostructures were fabricated on the Zr-based MG surface, resulting in surface superhydrophilicity.

(2) After low-temperature annealing treatment, the laser-ablated surfaces were transformed from superhydrophilic to superhydrophobic.

(3) The contact angle of the superhydrophobic surface was affected by the spot interval (*SI*), and the maximum contact angle reached 166° when the *SI* was 50 μm. When increasing the *SI* from 50 to 130 μm, the sliding angle of the superhydrophobic surface increased from 2° to 180°, and correspondingly, the surface adhesion force increased from 18.7 to 58.5 μN.

(4) By analyzing its surface structures and chemical composition, the superhydrophobicity of the laser-ablated surface after annealing was related to the formation of hierarchical micro/nanostructures as well as the absorption of organic compounds with low surface free energy in air, and the difference in surface adhesion force was mainly ascribed to the difference in surface roughness.

(5) It was demonstrated that a superhydrophobic surface with a low adhesion force could be used in a self-cleaning application and that superhydrophobic surfaces with different adhesion forces could be applied in no-loss liquid transportation.

ASSOCIATED CONTENT

Supporting information

Schematic diagram illustrating the nanosecond laser machining system and processing path; typical measurement processes of the adhesion force; schematic diagram illustrating the possible formation mechanisms of nanoparticles and ripples; 3D topographies of the laser-ablated surfaces obtained under different *SI*s; the CAs of the laser-ablated surfaces obtained under different *SI*s and the CA of the polished surface; the CAs of the laser-ablated surfaces obtained after annealing under different *SI*s and the CA of the polished surface after annealing; the optical images showing the measurement processes of the CA under different *SI*s; XPS results of surface element content (at.%).

Movies S1 and 2 showing the dynamic change process of a water droplet with 5 μL falling on 20 mm × 20 mm superhydrophilic surface (*SI* = 50 μm).

AUTHOR INFORMATION

Corresponding Author

*E-mail address: huanghu@jlu.edu.cn.

ACKNOWLEDGMENTS

This work was supported by the National Natural Science Foundation of China (Grant No. 51705197), the Graduate Innovation Fund of Jilin University (Grant No. 101832020CX106), and the Fundamental Research Funds for the Central Universities (2019-2022).

REFERENCES

(1) Darmanin, T.; Guittard, F. Superhydrophobic and Superoleophobic Properties in Nature. *Mater. Today* **2015,** *18,* 273-285.

(2) Barthlott, W.; Neinhuis, C. Purity of the Sacred Lotus, or Escape from Contamination in Biological Surfaces. *Planta* **1997,** *202*, 1-8.

(3) Feng, L.; Zhang, Y. N.; Xi, J. M.; Zhu, Y.; Wang, N.; Xia, F.; Jiang, L. Petal Effect: A Superhydrophobic State with High Adhesive Force. *Langmuir* **2008,** *24*, 4114-4119.

(4) Pan, R.; Zhang, H. J.; Zhong, M. L. Triple-Scale Superhydrophobic Surface with Excellent Anti-Icing and Icephobic Performance via Ultrafast Laser Hybrid Fabrication. *ACS Appl. Mater. Interfaces* **2021,** *13*, 1743-1753.

(5) Rad, S. V.; Moosavi, A.; Nouri-Boroujerdi, A.; Najafkhani, H.; Najafpour, S. Drag Reduction in Internal Turbulent Flow by Fabricating Superhydrophobic Al_2O_3/Waterborne Polyurethane Coatings. *Surf. Coat. Technol.* **2021,** *421*, 127406.

(6) Liu, S. Q.; Zhang, X. T.; Seeger, S. Solvent-Free Fabrication of Flexible and Robust Superhydrophobic Composite Films with Hierarchical Micro/Nanostructures and Durable Self-Cleaning Functionality. *ACS Appl. Mater. Interfaces* **2019,** *11*, 44691-44699.

(7) Hong, X.; Gao, X. F.; Jiang, L. Application of Superhydrophobic Surface with High Adhesive Force in No Lost Transport of Superparamagnetic Microdroplet. *J. Am. Chem. Soc.* **2007,** *129*, 1478-1479.

(8) Liu, J. Y.; Song, J.; Wang, G. S.; Chen, F. Z.; Liu, S.; Yang, X. L.; Sun, J.; Zheng, H. X.; Huang, L.; Jin, Z. J.; Liu, X. Maskless Hydrophilic Patterning of the Superhydrophobic Aluminum Surface by an Atmospheric Pressure Microplasma Jet for Water Adhesion Controlling. *ACS Appl. Mater. Interfaces* **2018,** *10*, 7497-7503.

(9) Wu, D.; Wu, S. Z.; Chen, Q. D.; Zhang, Y. L.; Yao, J.; Yao, X.; Niu, L. G.; Wang, J. N.; Jiang, L.; Sun, H. B. Curvature-Driven Reversible in Situ Switching between Pinned and Roll-Down Superhydrophobic States for Water Droplet Transportation. *Adv. Mater.* **2011,** *23*, 545-549.

(10) Sarac, B.; Eckert, J. Thermoplasticity of Metallic Glasses: Processing and Applications. *Prog. Mater Sci.* **2022,** *127*, 100941.

(11) Savaedi, Z.; Motallebi, R.; Mirzadeh, H.; Malekan, M. Superplasticity of Bulk Metallic Glasses (BMGs): A Review. *J. Non-Cryst. Solids* **2022,** *583*, 121503.

(12) Jia, H. L.; Wang, G. Y.; Chen, S. Y.; Gao, Y. F.; Li, W. D.; Liaw, P. K. Fatigue and

Fracture Behavior of Bulk Metallic Glasses and their Composites. *Prog. Mater Sci.* **2018,** *98*, 168-248.

(13) Zhang, M.; Sun, J.; Wang, Y. J.; Yu, M. M.; Liu, F.; Ding, G. Z.; Zhao, X. J.; Liu, L. Preparation of Stable and Durable Superhydrophobic Surface on Zr-Based Bulk Metallic Glass. *Colloids Surf., A* **2021,** *631*, 127654.

(14)Ma, J.; Zhang, X. Y.; Wang, D. P.; Zhao, D. Q.; Ding, D. W.; Liu, K.; Wang, W. H. Superhydrophobic Metallic Glass Surface with Superior Mechanical Stability and Corrosion Resistance. *Appl. Phys. Lett.* **2014,** *104*, 173701.

(15) Wang, Q. H.; Cheng, Y. Y.; Zhu, Z. X.; Xiang, N.; Wang, H. X. Modulation and Control of Wettability and Hardness of Zr-Based Metallic Glass via Facile Laser Surface Texturing. *Micromachines* **2021,** *12*, 1322.

(16) Zhu, S.; Bian, Y.; Wu, T.; Chen, C.; Jiao, Y.; Jiang, Z.; Huang, Z.; Li, E.; Li, J.; Chu, J.; Hu, Y.; Wu, D.; Jiang, L. High Performance Bubble Manipulation on Ferrofluid-Infused Laser-Ablated Microstructured Surfaces. *Nano Lett.* **2020,** *20*, 5513-5521.

(17) Jiang, S.; Hu, Y.; Wu, H.; Zhang, Y.; Zhang, Y.; Wang, Y.; Zhang, Y.; Zhu, W.; Li, J.; Wu, D.; Chu, J. Multifunctional Janus Microplates Arrays Actuated by Magnetic Fields for Water/Light Switches and Bio-Inspired Assimilatory Coloration. *Adv. Mater.* **2019,** *31*, 1807507.

(18) Huang, H.; Qian, Y. F.; Wang, C.; Yan, J. W. Laser Induced Micro-Cracking of Zr-Based Metallic Glass Using 10^{11} W/m^2 Nano-Pulses. *Mater. Today. Commun.* **2020,** *25*, 101554.

(19) Takayama, N.; Yan, J. W. Mechanisms of Micro-Groove Formation on Single-Crystal Diamond by a Nanosecond Pulsed Laser. *J. Mater. Process. Technol.* **2017,** *243*, 299-311.

(20) Wang, C.; Huang, H.; Qian, Y. F.; Zhang, Z. Y.; Yan, J. W. One-Step Fabrication of Regular Hierarchical Micro/Nano-Structures on Glassy Carbon by Nanosecond Pulsed Laser Irradiation. *J. Manuf. Processes* **2021,** *62*, 108-118.

(21) Lou, K.; Qian, S.-X.; Wang, X.-L.; Li, Y. N.; Gu, B.; Tu, C. H.; Wang, H.-T. Two-Dimensional Microstructures Induced by Femtosecond Vector Light Fields on Silicon. *Opt.*

Express **2012,** *20*, 120-127.

(22) Zhang, R.; Huang, C. Z.; Wang, J.; Feng, S. C.; Tao, H. Evolution of Micro/Nano-Structural Arrays on Crystalline Silicon Carbide by Femtosecond Laser Ablation. *Mater. Sci. Semicond. Process.* **2021,** *121*, 105299.

(23) Karlash, A.; Dmytruk, A.; Dmitruk, I.; Berezovska, N.; Hrabovskyi, Y.; Blonskyi, I. Impact of Wavelength, Intensity and Polarization on the Morphology of Femtosecond Laser‐Induced Structures on Crystalline Silicon Surface. *Appl. Nanosci.* **2022,** *12*, 1191–1199.

(24) Guan, Y. C.; Zhou, W.; Li, Z. L.; Zheng, H. Y.; Lim, G. C.; Hong, M. H. Femtosecond Laser-Induced Ripple Structures on Magnesium. *Appl. Phys. A: Mater. Sci. Process.* **2014,** *115*, 13-18.

(25) Wenzel, R. Resistance of Solid Surfaces to Wetting by Water. *Ind. Eng. Chem.* **1936,** *28*, 988-994.

(26) Yang, C.-Y.; Mei, X.-S.; Tian, Y.-L.; Zhang, D.-W.; Li, Y.; Liu, X.-P. Modification of Wettability Property of Titanium by Laser Texturing. *Int. J. Adv. Manuf. Technol.* **2016,** *87*, 1663-1670.

(27) Li, X. Y.; Jiang, Y.; Jiang, Z. H.; Li, Y. C.; Wen, C. E.; Lian, J. S. Reversible Wettability Transition between Superhydrophilicity and Superhydrophobicity through Alternate Heating-Reheating Cycle on Laser-Ablated Brass Surface. *Appl. Surf. Sci.* **2019,** *492*, 349-361.

(28) Cao, Z.; Ouyang, Z. Q.; Liu, Z. Y.; Li, Y.; Ouyang, Y. X.; Lin, J. H.; Xie, X. Z.; Long, J. Y. Effects of Surface Oxides and Nanostructures on the Spontaneous Wettability Transition of Laser-Textured Copper Surfaces. *Appl. Surf. Sci.* **2021,** *560*, 150021.

(29) Cassie, A.; Baxter, S. Wettability of Porous Surfaces. *Trans. Faraday Soc.* **1944,** *40*, 546-551.

(30) Long, J. Y.; Fan, P. X.; Gong, D. W.; Jiang, D. F.; Zhang, H. J.; Li, L.; Zhong, M. L. Superhydrophobic Surfaces Fabricated by Femtosecond Laser with Tunable Water Adhesion: from Lotus Leaf to Rose Petal. *ACS Appl. Mater. Interfaces* **2015,** *7*, 9858-65.

(31) Jiao, Y.; Brousseau, E.; Shen, X. Y.; Wang, X. X.; Han, Q. Q.; Zhu, H. X.; Bigot,

S.; He, W. F. Investigations in the Fabrication of Surface Patterns for Wettability Modification on a Zr-Based Bulk Metallic Glass by Nanosecond Laser Surface Texturing. *J. Mater. Process. Technol.* **2020,** *283*, 116714.

(32) Miyauchi, M.; Nakajima, A.; Watanabe, T.; Hashimoto, K. Photocatalysis and Photoinduced Hydrophilicity of Various Metal Oxide Thin Films. *Chem. Mater.* **2002,** *14*, 2812-2816.

(33) Zhang, H. Y.; Qian, Y. F.; Zhang, L.; Zhang, D.; Liu, H. L.; Huang, H. Surface Coloration of Zr-Based Metallic Glass by Nanosecond Pulsed Laser Irradiation in Ambient Atmosphere. *Mater. Lett.* **2021,** *304*, 130721.

(34) Park, S. H.; Lim, K. R.; Na, M. Y.; Kim, K. C.; Kim, W. T.; Kim, D. H. Effect of Minor Addition of Zr on the Oxidation Behavior of Ti-Cu Metallic Glasses. *Met. Mater. Int.* **2016,** *22*, 229-235.

(35) Zhang, M.; Gong, P.; Li, N.; Zheng, G. P.; Deng, L.; Jin, J. S.; Li, Q. M.; Wang, X. Y. Oxidation Behavior of a $Ti_{16.7}Zr_{16.7}Hf_{16.7}Cu_{16.7}Ni_{16.7}Be_{16.7}$ High-Entropy Bulk Metallic Glass. *Mater. Lett.* **2019,** *236*, 135-138.

(36) Zhang, M.; Zhang, J. C.; Deng, L.; Li, Q. M.; Jin, J. S.; Wang, X. Y. Microstructure Evolution of Bulk Metallic Glass During Thermal Oxidation under Plastic Strain. *Corros. Sci.* **2019,** *147*, 192-200.

(37) Lim, K. R.; Kim, C. E.; Yun, Y. S.; Kim, W. T.; Soon, A.; Kim, D. H. Remarkably Stable Amorphous Metal Oxide Grown on Zr-Cu-Be Metallic Glass. *Sci. Rep.* **2015,** *5*, 1-8.

(38) Chang, F.-M.; Cheng, S.-L.; Hong, S.-J.; Sheng, Y.-J.; Tsao, H.-K. Superhydrophilicity to Superhydrophobicity Transition of CuO Nanowire Films. *Appl. Phys. Lett.* **2010,** *96*, 114101.

(39) Ta, D. V.; Dunn, A.; Wasley, T. J.; Kay, R. W.; Stringer, J.; Smith, P. J.; Connaughton, C.; Shephard, J. D. Nanosecond Laser Textured Superhydrophobic Metallic Surfaces and their Chemical Sensing Applications. *Appl. Surf. Sci.* **2015,** *357*, 248-254.

(40) Chun, D.-M.; Ngo, C.-V.; Lee, K.-M. Fast Fabrication of Superhydrophobic Metallic Surface Using Nanosecond Laser Texturing and Low-Temperature Annealing. *CIRP Ann. Manuf. Technol.* **2016,** *65*, 519-522.

(41) Jagdheesh, R.; Hauschwitz, P.; Mužík, J.; Brajer, J.; Rostohar, D.; Jiříček, P.; Kopeček, J.; Mocek, T. Non-Fluorinated Superhydrophobic Al7075 Aerospace Alloy by Ps Laser Processing. *Appl. Surf. Sci.* **2019,** *493*, 287-293.

(42) Yang, Z.; Liu, X. P.; Tian, Y. L. Insights into the Wettability Transition of Nanosecond Laser Ablated Surface under Ambient Air Exposure. *J. Colloid Interface Sci.* **2019,** *533*, 268-277.

(43) Li, H. Y.; Li, N.; Zuo, P. P.; Qu, S. J.; Shen, W. Z. Efficient Adsorption-Reduction Synergistic Effects of Sulfur, Nitrogen and Oxygen Heteroatom Co-Doped Porous Carbon Spheres for Chromium (VI) Removal. *Colloids Surf., A* **2021,** *618*, 126502.

(44) Long, J. Y.; Zhong, M. L.; Zhang, H. J.; Fan, P. X. Superhydrophilicity to Superhydrophobicity Transition of Picosecond Laser Microstructured Aluminum in Ambient Air. *J. Colloid Interface Sci.* **2015,** *441*, 1-9.

(45) Khorsand, S.; Raeissi, K.; Ashrafizadeh, F.; Arenas, M. A. Super-Hydrophobic Nickel-Cobalt Alloy Coating with Micro-Nano Flower-Like Structure. *Chem. Eng. J.* **2015,** *273*, 638-646.

(46) Niu, C. N.; Han, J. Y.; Hu, S. P.; Chao, D. Y.; Song, X. G.; Howlader, M. M. R.; Cao, J. Fast and Environmentally Friendly Fabrication of Superhydrophilic-Superhydrophobic Patterned Aluminum Surfaces. *Surf. Interfaces* **2021,** *22*, 100830.

(47) Huang, J. Y.; Yang, S. Investigation on Anisotropic Tribological Properties of Superhydrophobic/Superlipophilic Lead Bronze Surface Textured by Femtosecond Laser. *Appl. Surf. Sci.* **2022,** *579*, 152223.

(48) Pandiyaraj, K. N.; Selvarajan, V.; Deshmukh, R. R.; Gao, C. Y. Modification of Surface Properties of Polypropylene (PP) Film Using DC Glow Discharge Air Plasma. *Appl. Surf. Sci.* **2009,** *255*, 3965-3971.

(49) Cao, Q. H.; Wang, Z. S.; He, W. T.; Guan, Y. C. Fabrication of Superhydrophilic Surface on Alumina Ceramic by Ultrafast Laser Microprocessing. *Appl. Surf. Sci.* **2021,** *557*, 149842.

(50) Li, X. C.; Liu, R. J.; Li, X. N.; Gao, K.; Wu, J. C.; Gong, D. D.; Jia, P. Y. Large-Scale Surface Modification to Improve Hydrophilicity Through Using a Plasma Brush

Operated at One Atmospheric Pressure. *Phys. Plasmas* **2019,** *26*, 023510.

(51) Krylova, V.; Dukštienė, N.; Lelis, M.; Tučkutė, S. PES/PVC Textile Surface Modification by Thermo-Chemical Treatment for Improving its Hydrophilicity. *Surf. Interfaces* **2021,** *25*, 101184.

Supporting information

Achieving Superhydrophobicity of Zr-Based Metallic Glass Surfaces with Tunable Adhesion by Nanosecond Laser Ablation and Annealing

Mingming Cui[1], *Hu Huang*[1]*, *Chao Wang*[1], *Lin Zhang*[2], *Jiwang Yan*[2]

[1]Key Laboratory of CNC Equipment Reliability, Ministry of Education, School of Mechanical and Aerospace Engineering, Jilin University, Changchun, Jilin, 130022, China

[2]Department of Mechanical Engineering, Faculty of Science and Technology, Keio University, Yokohama 223-8522, Japan

*E-mail address: huanghu@jlu.edu.cn.

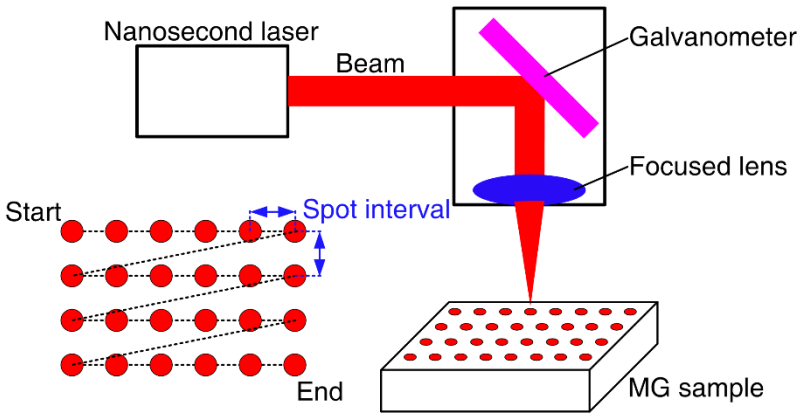

Figure S1. Schematic diagram illustrating the nanosecond laser machining system and processing path.

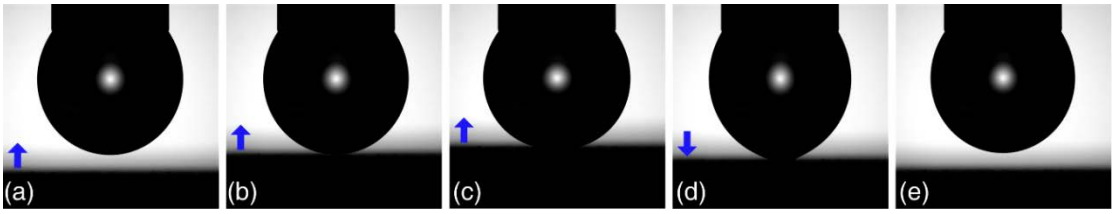

Figure S2. Typical measurement processes of the adhesion force: (a) the superhydrophobic surface is moved up to approach the water droplet, (b) the superhydrophobic surface is initially in contact with the water droplet, (c) the superhydrophobic surface is further moved up to compress the water droplet, (d) the superhydrophobic surface is moved down to stretch the water droplet, and (d) the superhydrophobic surface is completely separated from the water droplet.

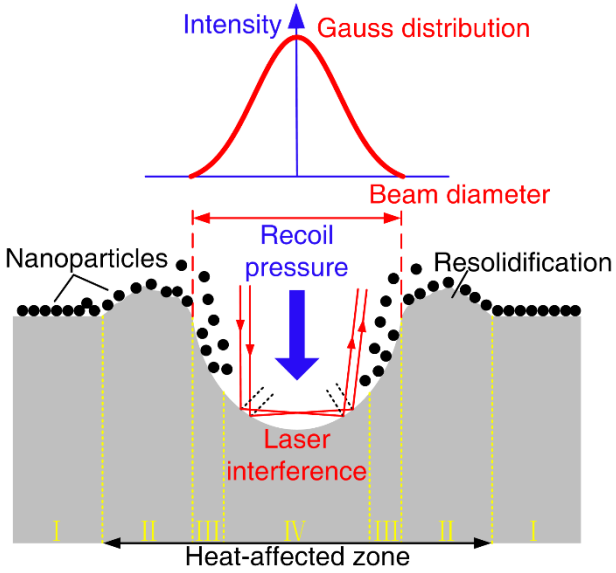

Figure S3. Schematic diagram illustrating the possible formation mechanisms of nanoparticles and ripples.

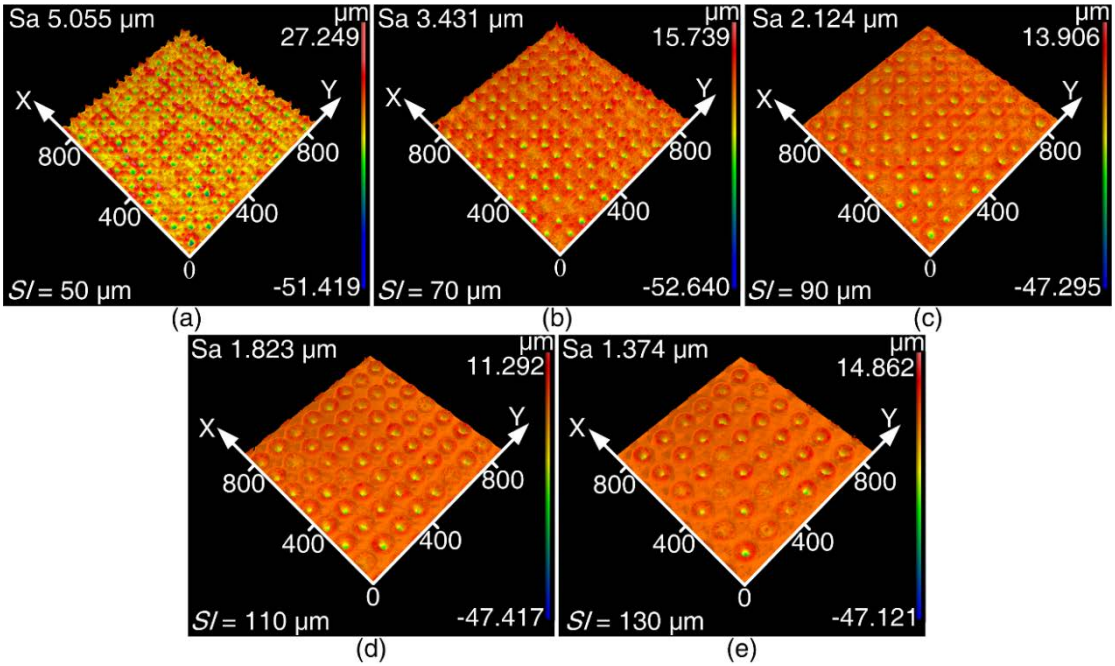

Figure S4. 3D topographies of the laser-ablated surfaces obtained under different *SI*s: (a) *SI* = 50 µm, (b) *SI* = 70 µm, (c) *SI* = 90 µm, (d) *SI* = 110 µm, and (e) *SI* = 130 µm.

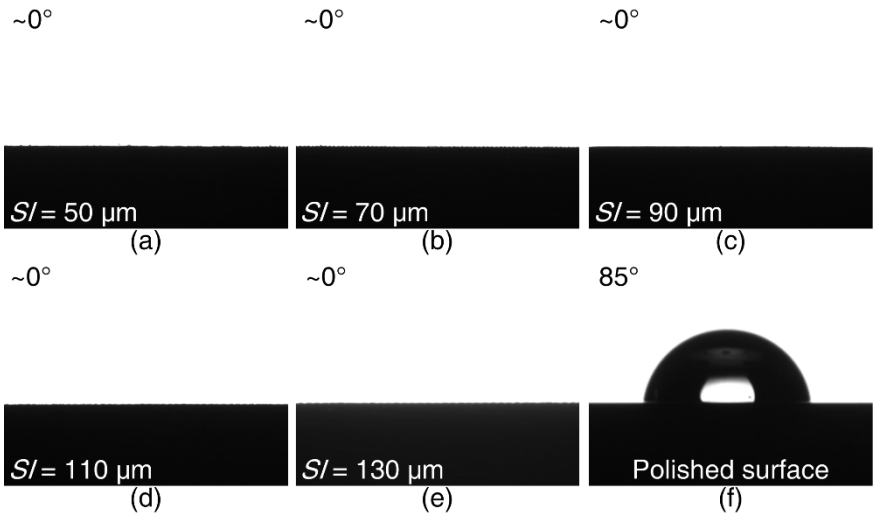

Figure S5. The CAs of the laser-ablated surfaces obtained under different *SI*s: (a) *SI* = 50 µm, (b) *SI* = 70 µm, (c) *SI* = 90 µm, (d) *SI* = 110 µm, and (e) *SI* = 130 µm. (f) The CA of the polished surface.

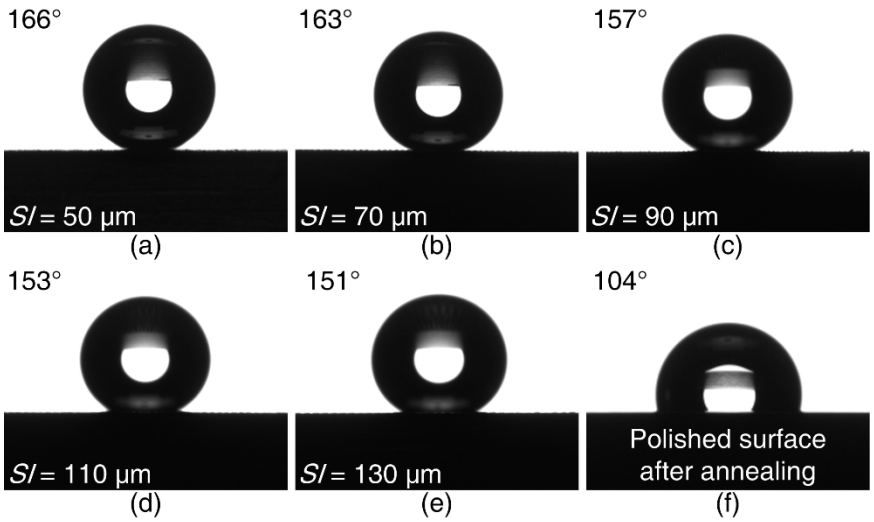

Figure S6. The CAs of the laser-ablated surfaces obtained after annealing under different *SI*s: (a) *SI* = 50 µm, (b) *SI* = 70 µm, (c) *SI* = 90 µm, (d) *SI* = 110 µm, and (e) *SI* = 130 µm. (f) The CA of the polished surface after annealing.

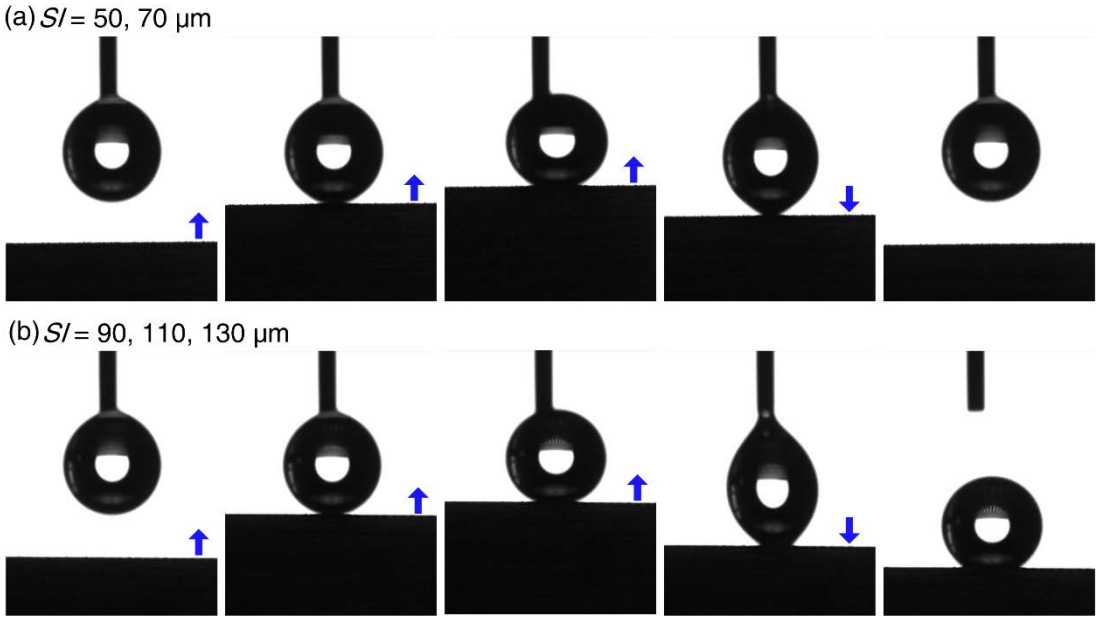

Figure S7. The optical images showing the measurement processes of the CA under different *SI*s: (a) *SI* = 50, 70 µm, and (b) *SI* = 90, 110, 130 µm.

Table S1. XPS results of surface element content (at.%).

Element	*SI* = 50 μm (after annealing)	*SI* = 50 μm (before annealing)	Polished surface after annealing	Polished surface before annealing
C	33.59±0.91	27.10±0.34	31.71±0.44	26.71±0.48
O	45.98±0.35	51.21±0.39	49.60±0.76	52.45±0.60
Zr	2.53±0.15	3.40±0.09	12.51±0.25	13.61±0.18
Ti	2.35±0.13	2.51±0.06	4.28±0.24	4.42±0.23
Cu	12.11±0.28	12.36±0.37	1.17±0.18	1.58±0.29
Ni	3.44±0.20	3.42±0.19	0.73±0.17	1.23±0.16